RESEARCH ARTICLE

Key Points:
- New experimental data on fracture stress-dependent flow and stiffness are presented for two natural fractures from a fault damage zone
- Differences in fracture stiffness and flow properties are explained by variations in fracture aperture and contact ratio distribution
- An active chemical altered fracture shows higher flow rate compared to the well-mated unaltered fracture that closes during loading

Correspondence to:
E. Skurtveit,
esk@ngi.no

Experimental Investigation of Natural Fracture Stiffness and Flow Properties in a Faulted CO₂ Bypass System (Utah, USA)

Elin Skurtveit[1,2] (iD), Anja Sundal[2] (iD), Tore Ingvald Bjørnarå[1] (iD), Magnus Soldal[1,2] (iD), Guillaume Sauvin[1], Valentin Zuchuat[2] (iD), Ivar Midtkandal[2] (iD), and Alvar Braathen[2] (iD)

[1]Norwegian Geotechnical Institute, Oslo, Norway, [2]Department of Geosciences, University of Oslo, Oslo, Norway

Abstract Fracture stiffness and flow properties have been measured in the laboratory using naturally fractured fault rock samples from the Little Grand Wash fault, Utah, USA. We compare fracture closure and related flow change during isotropic loading of two fractures which have been subject to various amounts of paleoreactive flow. The two tested fractures are described as (i) a small-aperture fracture (0.1 mm) with negligible geochemical alterations of the fracture surface and (ii) a large-aperture fracture (0.53 mm) where precipitates are observed on the fracture surface. X-ray imaging is used for quantification of fracture aperture and fracture surface contact distribution. The petrographical characterization using scanning electron microscopy and X-ray powder diffraction is performed pretest and describes burial and uplift diagenesis as well as pulses of reactive fluid flow within the fault. The stress-dependent flow and deformation experiment provides new data on fracture stiffness and flow for naturally developed fractures in siliciclastic rock. Fracture stiffness is found to be highest for the small-aperture fracture due to its high-fracture contact ratio and well-developed surface mating during closure. For the naturally altered and rougher, large-aperture fracture, fracture stiffness is lower and a highly stress dependent decay in flow is observed during initial closure. The results illustrate that a natural fracture with high contact ratio and well-mated surfaces will close during loading, whereas a fracture associated with high flow rates and affected by previous geochemical alteration maintains a high flow rate compared to the host rock during similar loading.

1. Introduction

Seal integrity during operations that inject fluids in to permeable rocks is a topic of great interest, especially in the CO_2 storage community, and is also of relevance for wastewater injection and reservoir pressure support. Large efforts are made to identify safe operation limits (e.g., Bohloli et al., 2017) and toward understanding critical areas for failure, such as fault zones (e.g., Skurtveit et al., 2018). Faults are challenging as their sealing properties within subsurface reservoir-seal systems cannot be directly observed. Accordingly, knowledge has been gained from field observations that can document structural impact such as cataclastic deformation (Fossen et al., 2007), clay smear (Vrolijk et al., 2016), and cementation (Eichhubl et al., 2009). Further, seal bypass systems such as fracture corridors (Ogata et al., 2014), consisting of mainly tensile fractures that are closely spaced within localized tabular zones, have been identified as critical structures. Understanding fluid transport properties within such fracture corridors is important for quantifying vertical migration of fluids within a faulted reservoir seal system and in the evaluation of seal integrity.

The Jurassic Entrada Sandstone (Peterson, 1988) at Little Grand Wash (LGW) in Central Utah, USA, is an exhumed paleoreservoir showing evidence of CO_2-rich fluid accumulations in the geological past (Frery et al., 2015, 2017; Kampman et al., 2014). It provides an excellent field location for studying seal bypass systems in a siliciclastic sedimentary succession (Busch et al., 2014; Midtkandal et al., 2018). Migration of CO_2- and/or CH_4-rich groundwaters causes bleaching (i.e., reduction of Fe (III) and/or dissolution of Fe-oxides) of aeolian sandstone (reservoir) and siltstone (seal) layers that were originally stained red by hematite or goethite (e.g., Beitler et al., 2005; Chan et al., 2000; Eichhubl et al., 2009; Garden et al., 2001; Wigley et al., 2012). Bleaching patterns are easily observed in the field and allow for identification of relict fluid pathways related to faults and fracture corridors (Ogata et al., 2014; Skurtveit et al., 2017; Sundal et al., 2017).

The LGW fault is an approximately WNW-ESE trending fault with a normal, down-south throw of 150–250 m (Campbell & Baer, 1978), and the CO_2 leakage system is described in several works (e.g., Gratier et al., 2012; Jung et al., 2014; Naruk et al., 2019; Shipton et al., 2004). Detailed geochemical analysis of fluid inclusions points to a CO_2-rich migrating fluid in the Green River area (Kampman et al., 2014; Wigley et al., 2012), while dated travertine deposits document 400.000 years of CO_2-rich fluid expulsion, degassing, and deposition at the surface (Evans et al., 2004). Detailed $\delta^{13}C$ and $\delta^{18}O$ data sets identify a pulsating system with several cycles of sealing-dissolution-sealing and total leakage estimated as less than 900 kg/year (Frery et al., 2015, 2017).

Although a well-studied area, there are few measurements of mechanical properties and permeability for the LGW Fault in the Entrada Sandstone, which can document impacts of the relict CO_2 fluid system on basic mechanical and flow properties (Espinoza et al., 2018; Major et al., 2018). Effects of chemical alteration in rock material with low permeability are challenging to document and quantify in experimental work due to slow reaction kinetics. However, using natural analogs for CO_2 storage provides an opportunity for experimental measurements of flow properties and mechanical changes in naturally fractured sealing units exposed to CO_2-charged brine over geological time, as well as comparison with nonaltered and intact samples from the same system. In the current work, Entrada Sandstone core samples retrieved from a research well in the footwall damage zone of the LGW fault (Kampman et al., 2014) are used for measuring natural fracture stiffness (closure) and flow properties for vertical, open mode fractures in the leaking fault damage zone (Naruk et al., 2019). Access to two natural fractures from the same stratigraphic unit, but with different signs of alteration induced by fluid-mineral reactions during paleoflux, allows for novel experimental investigation of the role of past reactive flow on intrinsic, stress-dependent flow properties. The natural opening mode fractures were not separated before nor during the experimental work, providing representative aperture, stiffness, and flow rates for the LGW fault zone. Intact core sample from the same zone gives host rock reference properties for comparison. Pretest mineralogical and microstructural analysis of the fracture surface and host rock provides detailed observations of the paleo fluid-rock alteration, whereas X-ray computer tomography is used for visualization of fracture aperture. The stress-dependent fracture closure and flow reduction is described using a stiffness-flow relationship demonstrating variations related to fracture development and relict geochemical alterations within the fracture.

2. Fracture Flow and Stiffness

The fluid flow in a fracture is most commonly conceptualized as the flow between two parallel plates and the fracture transmissivity T (m^3) is cubic in aperture b (m); hence, cubic law (e.g., Rutqvist & Stephansson, 2003; Witherspoon et al., 1980):

$$T = \frac{b^3}{12} \tag{1}$$

The aperture may be separated into a physical (mechanical) aperture b_M (m) and a hydraulic aperture b_H (m). There is an important distinction between the two apertures: The mechanical aperture is the actual opening of the fracture and accounts for the fracture void volume, while the hydraulic aperture is the interconnected aperture contributing to the flow along the fracture and accounts for the effective transmissivity through the cubic law (Equation 1). Using the transmissivity, Darcy's law can be modified to express the volumetric flow rate, Q, through a smooth fracture with hydraulic aperture as follows:

$$Q = \frac{b_H^3 w}{12\mu} \frac{\Delta p}{L} \tag{2}$$

where μ (Pa s) is the fluid viscosity, w (m) is the width of the fracture, and Δp (Pa) is the pressure drop over the length L (m) of the fracture. Because natural fractures do not exhibit perfectly flat surfaces, the hydraulic aperture is always smaller than the mechanical aperture. There are many theories that correlate the two types of aperture by using various conceptual descriptions of a fracture and accounting for various features of fractures such as asperity and roughness (e.g., Dippenaar & Van Rooy, 2016; Huo & Benson, 2015; Witherspoon et al., 1980). Another approach is the concept of the joint roughness coefficient (JRC), by Barton and Choubey (1977), applied for the fracture logging in this study.

A common relationship between the hydraulic aperture b_H and the mechanical aperture b_M is the conceptual model defined by Walsh (1981):

$$b_H^3 = b_M^3 \frac{(1 - R_c)}{(1 + R_c)} \tag{3}$$

where the R_c (−) represents the contact area ratio defined as follows:

$$R_c = \frac{A_c}{A} \tag{4}$$

and A_c (m^2) is the area of the contact between the fracture faces and A (m^2) is the surface area of the fracture. From the correlation in Equation 3 it can be seen that when $R_c = 0$ then $b_H = b_M$; thus, this approach ignores other effects on hydraulic aperture such as roughness of the fracture surface.

Fracture normal stiffness K_n (Pa/m) is a geometry-dependent mechanical property which describes the stress-dependent normal closure of a fracture and is defined as the ratio of the change in effective normal stress σ'_n (Pa) and change in fracture aperture b (m) (Jaeger et al., 2009):

$$K_n = \frac{\Delta \sigma'_n}{\Delta b} \tag{5}$$

Pyrak-Nolte and Morris (2000) discuss the relationship between fracture stiffness and fracture geometry numerically based on extensive experimental results. They suggest that the spatial distribution of apertures and contact areas provides the basis for a fracture stiffness-flow relationship, and two main trends are identified: a rapid decrease in fluid flow with increasing stiffness related to the irregular distribution of aperture and contact points and a weak dependency of fluid flow on stiffness related to the uniformly distributed aperture and contact points. The work has resulted in a universal scaling relationship between fracture stiffness and fluid flow proposed in Pyrak-Nolte and Nolte (2016) for fracture deformation during application of stress. Simulations by (Lang et al., 2016) show a rapid, exponential stiffening of fractures when the contacts points are flattened by pressure dissolution compared to the linear stiffening expected for an unaltered fracture surface, suggesting that chemical alterations of fracture surfaces should be considered in a flow-stiffness relationship. Although simulations and conceptual models from stress-dependent flow are inspired by experimental observations, there is a need for more experimental work addressing natural fractures from a broader range of geological settings.

3. Samples and Fracture Characterization

3.1. Location and Sampling

The samples used for the experimental program in this study were collected from well CO_2W55 in silty, fine-grained sandstones of relatively low permeability in the upper Entrada Sandstone ("Earthy Member"). The CO_2W55 research well was drilled into the footwall damage zone of the LGW fault, Utah, USA (Kampman et al., 2013, 2014), and a cored succession of Entrada Sandstone was logged between 10 and 100 m (Figure 1). Six sedimentary facies are recognized (Appendix A), and their assemblage patterns are used to establish two sedimentary subenvironments, here listed as facies associations (FA): (1) wet interdune deposits and (2) aeolian dune deposits. The coarser dune deposits display an overall paler or more bleached color than the very fine-grained, red-colored intradune deposits. Fracture frequency ranges from 0 to 3 fractures per meter, and natural, subvertical opening mode fractures with no indications of shear movement dominate the system. Measured JRC for open fractures is in the range of 6 to 13 following the method suggested by Barton and Choubey (1977). Overall, higher fracture densities (2–3 per meter) are associated with finer-grained interdune deposits (FA 1, Facies A, B, C) and a pale red color with local bleaching along fractures.

Two couplets of fracture and host rock samples were selected for experimental investigation of fracture stiffness and stress-dependent flow properties. The first couplets, LGW1 and LGW2, are from the red, silty sandstone interval at 24.7 m core depth, recognized as FA 1, Facies B. Sample LGW1 contains a natural, partly open fracture that is not separated during plug preparation, whereas LGW2 is the reference intact host
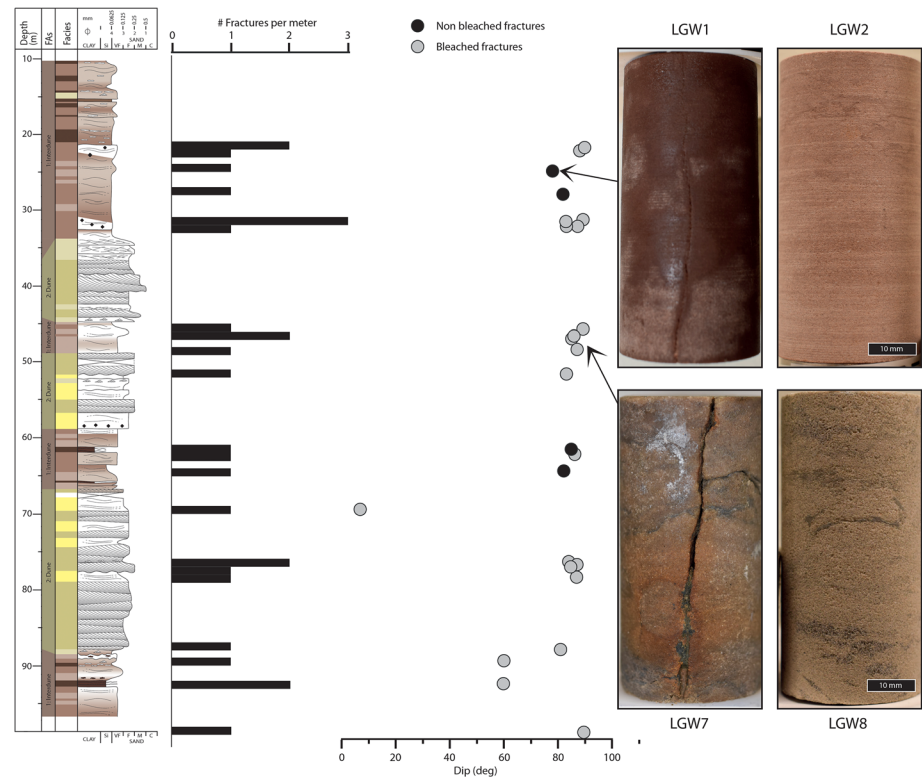
Figure 1. Core log from the Entrada Sandstone succession in well CO₂W55 showing the interpreted distribution of sedimentary facies by color code (detailed description for all Facies A through F can be found in Appendix A) and the two facies associations (FAs) 1: Wet interdune, 2: Aeolian dunes. The number of fractures per meter and the fracture dips are indicated in the log, as well as photographs and the location of the sample couplets LGW1 and LGW2 and LGW7 and LGW8 used for flow testing. All samples are collected from very fine to fine, silty sandstones (Facies B, FA1).

rock (Figure 1). The second couplets, samples LGW7 and LGW8, are from the pale-colored (bleached) fine-grained sandstone interval at 45.7 m log depth, FA 1, Facies B. Sample LGW7 comprises a naturally, wide fracture, partly cemented and held together with dark mineral precipitates within the fracture aperture, whereas LGW8 is a reference sample representing intact host rock from the same depth (Figure 1). An overview of the samples and matrix porosity estimated from intact plug dry volume is given in Table 1.

3.2. Methods of Characterization

Pretest material characterization targeted both the host rock properties and fracture surfaces in samples cut from the drilled core plugs used in flow experiments. X-ray powder diffraction (XRD) was performed using a Bruker D8 Advance instrument at the University of Oslo. Scanning Electron Microscopy (SEM) analyses were performed both on thin sections (2-D surface, 160 scan) from host rock samples and directly on the fracture surface (3-D whole rock sample) with a Hitachi SU5000 FE-SEM instrument at the University of Oslo. Chemical analysis and element mapping were performed using Energy Dispersive Spectroscopy (EDS) with a Dual Bruker Quantax XFlash 30 EDS system at the University of Oslo. Thin sections were carbon coated (Cressington 208C), and 3-D mounts were gold coated (Quorum Q150R) S. Host rock thin sections were cut from a core piece right below the core plug used for the experiment, oriented perpendicular to sedimentary lamina. The fracture surface samples (i.e., 3-D mounts used for SEM) were cut from a virgin part of the fracture right next to where the (fractured) core plugs (LGW1 and LGW7) were drilled.

Three thin sections (LGW1, LGW2, and LGW8) were analyzed at the Colorado School of Mines using automated SEM (automated mineralogy). Samples were loaded into a TESCAN-VEGA-3 Model LMU VP-SEM platform and analyzed by means of the control program TIMA3. Spectra from each point were acquired

Table 1
Sample List From Well CO$_2$W55 With Descriptions and Index Properties

Depth (m)	Sample ID	Sample description	Matrix porosity[a] (%)
24.77	LGW1	Narrow vertical opening mode fracture in red, very fine-grained, silty sandstone	
24.71	LGW2	Red reference sandstone	6.0
45.75	LGW7	Wide vertical opening mode fracture in pale-colored fine-grained sandstone, with silty laminas	
45.81	LGW8	Pale-colored reference sandstone	7.6

[a]Porosity estimated from dry weight and assuming quartz skeletal density of 2.66 g/cm^3 and not corrected for any salt precipitated during drying.

from four energy dispersive X-ray (EDX) spectrometers; the acceleration voltage is 24 keV, and the beam intensity 14. Monte Carlo simulations are applied to model interactions between the beam and the sample. Using a lookup table, a mineral or phase is assigned to each acquisition point and a compositional map generated in TIMA software.

Tomographic imaging of the fracture aperture was performed both before and after testing, using a Nikon Metrology industrial high-resolution 3-D computer tomography (CT) scanner equipped with a 225 kV microfocus X-ray tube. A tube voltage of 105 kV and tube current of 100 μA were used during image acquisition, and the voxel resolution is 30 μm. The 3-D images were reconstructed and visualized using VGStudio MAX by Visual Graphics, whereas Synopsys' Simpleware™ ScanIP (Simpleware™ScanIP, 2018) was used to segment the fracture aperture, generate a triangulated surface representation, and then calculate an average aperture measurement using a ray casting method (Inui et al., 2015). All CT images are processed with pores and fracture aperture displayed in white/light colors and with dense minerals appearing as dark areas.

3.3. Host Rock Characteristics

Grain-scale mineral distributions for small areas in thin section samples LGW1, LGW7, and LGW8 are shown in Figure 2, with relative fractions as quantified in TIMA (%) listed for comparison. The mineralogical characterization is supported by XRD analyses confirming relative silicate, carbonate, oxide, and sulfide distributions (Appendix B). The red-colored (not bleached) host rock sample LGW1 is quartz-rich (~60%), with 14% feldspar and 11% carbonate. The dominant grain size fraction is <100 μm, and the material is classified as silty to very fine sandstone (Facies B). The pale-colored (bleached) host rock of samples LGW7 and LGW8 is quartz dominated (64–73%) with 8–10% feldspar and 4.7–9.5% total carbonate. The average grain size is between 100 and 200 μm, that is, fine sand (Facies B). The total mount and composition of the carbonate cement varies between the red, unbleached sample (LGW1)) and the two bleached samples (LGW7 and LGW8). The lowest total carbonate content is found in LGW7 (4.7%), the bleached sample with fracture. Dolomitization is observed as zoned, scattered rhomboids. Hematite/magnetite contents (0.1%) are smaller in the bleached samples than in the red sample (0.5%). The pyrite content (0.5%) and relative amounts of TiO (0.4%) are larger in the fractured and bleached LGW7 sample, compared to the intact, bleached sample (LGW8). Pore-filling clays are similar for all samples and dominated by illite and muscovite/sericite, with some kaolinite and biotite. Grain coating illite is abundant. In LGW7, there are several fine layers and thus higher relative fractions of clay. Quartz overgrowths are frequent, despite abundant illite coating. Also, euhedral microquartz in illite-rich matrix is observed.

3.4. Fracture Characteristics

The fractures in samples LGW1 and LGW7 display some characteristic differences. The fracture in sample LGW1 appears as a thin hairline in the red, silty sandstone host rock (Figure 1). From the CT image (Figure 3a) the fracture appears to have several contact areas and bridges separating the fracture in an opening mode. A SEM image of the fracture surface (Figure 3a) from a separate sample below the tested fracture plug shows a fracture with roughness dominated by the grain size. Illitic grain coats stand out around grain molds, and authigenic calcite and barite crystals are observed on the fracture surface (Figure 3a). The fracture in sample LGW7 occurs within slightly coarser (fine sand) and more porous sandstone compared to
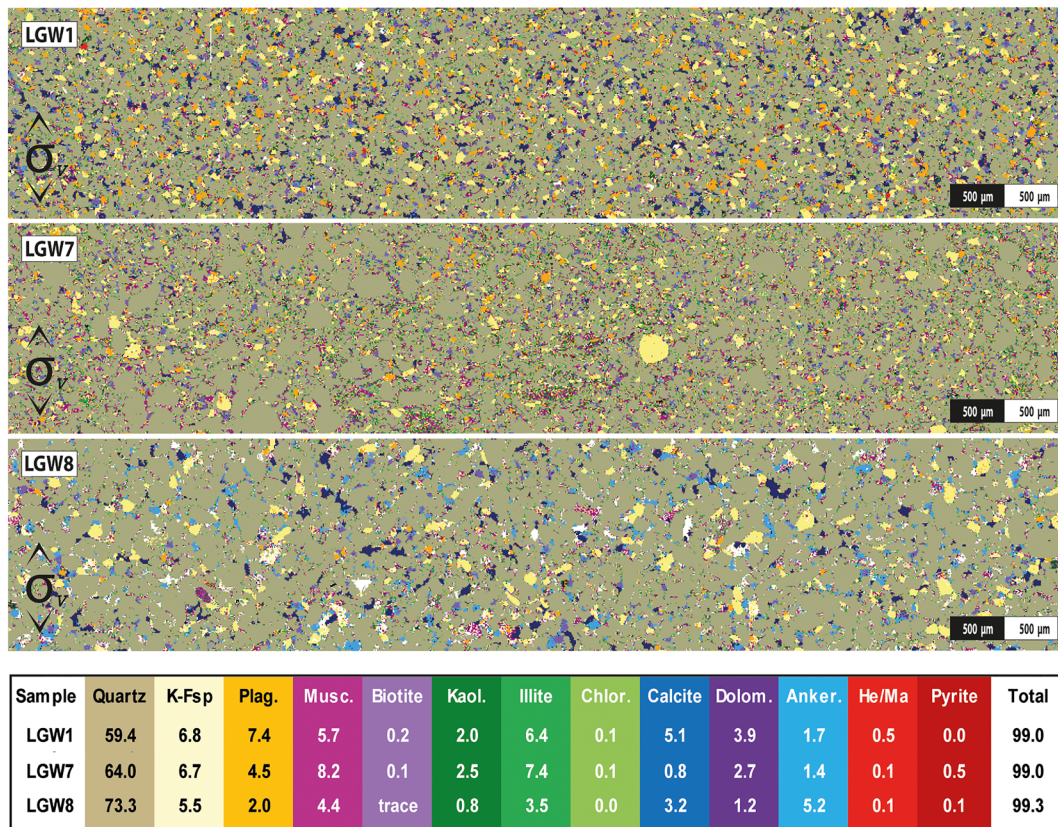
Sample	Quartz	K-Fsp	Plag.	Musc.	Biotite	Kaol.	Illite	Chlor.	Calcite	Dolom.	Anker.	He/Ma	Pyrite	Total
LGW1	59.4	6.8	7.4	5.7	0.2	2.0	6.4	0.1	5.1	3.9	1.7	0.5	0.0	99.0
LGW7	64.0	6.7	4.5	8.2	0.1	2.5	7.4	0.1	0.8	2.7	1.4	0.1	0.5	99.0
LGW8	73.3	5.5	2.0	4.4	trace	0.8	3.5	0.0	3.2	1.2	5.2	0.1	0.1	99.3

Figure 2. Rock matrix characteristics of samples LGW1 (core sample at 24.7 m, upper image), LGW7 (core sample at 45.8 m, middle image), and LGW8 (core sample at 45.8 m, lower image) shown in grain-scale mineralogy maps generated using TIMA software and automated scanning electron microscopy to produce an areal compositional map and relative fractions (%). Relative, color-coded mineral fractions (%) are listed in the table, and porosity is shown as white in images. For the two fractured samples LGW1 and LGW7 the thin section is cut approximately 5 mm away from the fracture surface and considered to represent host rock properties potentially affected by reactive paleofluids.

LGW1 and appears as a wide fracture with extensive mineral precipitation (Figure 3b). Frame work grains at the fracture surface are illite coated, as in LGW1, but diagenetic surface alterations are different, with euhedral crystals of both gypsum and pyrite observed (Figure 3b).

Fracture aperture and contact area are important but difficult parameters to quantify for the two fractures. Unconfined 3-D CT scans before and after the flow and stiffness testing are used as proxy and allows for comparison between the two fractures. A 2-D projection of the fracture aperture and a distribution of contact area R_c defined as mechanical aperture below CT scan resolution (Figure 4) show that LGW1 is a thin fracture with a mean mechanical aperture ranging from 0.1–0.09 mm and contact area from 36–59% for pretest to posttest CT scans, whereas LGW7 is a wide fracture with mean mechanical aperture in the range of 0.53–0.44 mm and contact area of 14–44% (Table 2). The range and distribution of fracture aperture are qualitatively considered a proxy for the fracture surface roughness, describing the LGW1 fracture as smoother than the wider LGW7 fracture.

CT images revealed clustering of a high-density mineral fill along the LGW7 fracture (Figure 3b). High-density mineral clustering is quantified by estimating the ratio of dense minerals within the fracture compared to the whole sample. The dense minerals are taken as number of voxels with CT values above the lower bond of the histogram peak. For LGW7 this ratio is close to 100% (Table 2), indicating that by far, most of the dense minerals occur along the fracture surface or in the host rock in close vicinity of the fracture. This clustering of mineral precipitates within the fracture supports a strong alteration of the LGW7 fracture compared to the LGW1 fracture, for which the very few dense minerals detected are distributed within the sample and cannot be related to the fracture.
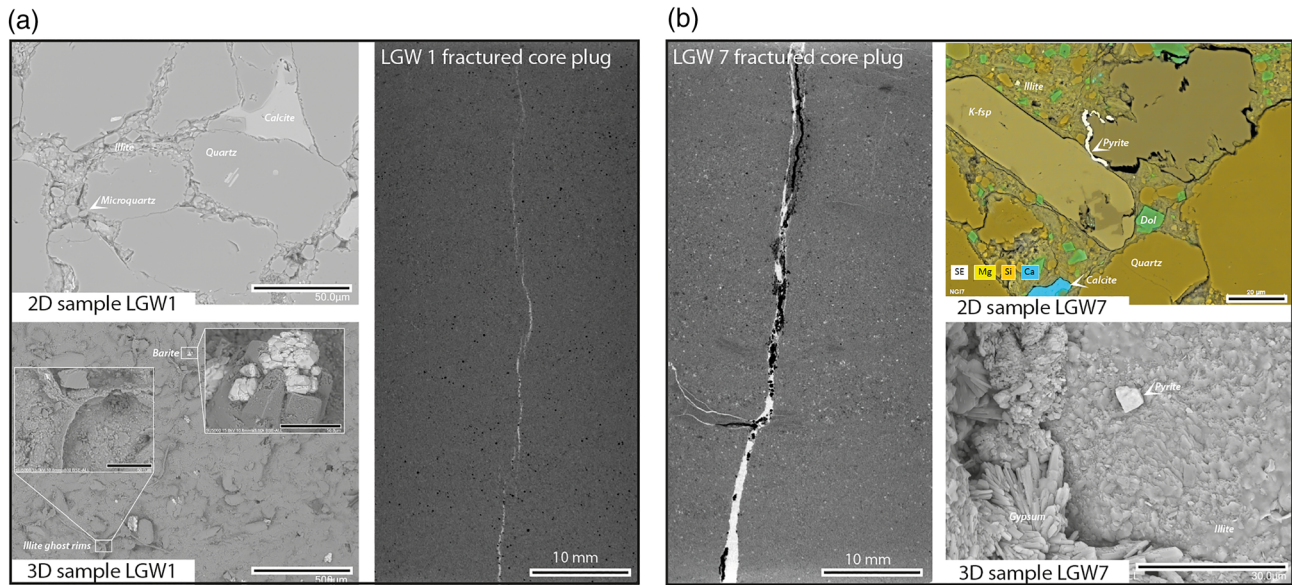
Figure 3. (a) Aperture of the LGW1 fracture defined by CT scan image (right) where aperture and pores as white/light colors and dense minerals are dark colored. Top left: Microtexture of LGW2 host rock matrix from 2-D thin section sample in SEM. Note calcite cement postquartz overgrowths. Bottom left: SEM image of 3-D fracture surface of LGW1. Note illite ghost rims and barite precipitates. (b) Aperture of the LGW7 fracture defined by CT scan image (left). Top right: SEM image with element coloring from LGW7 2-D thin section sample of rock matrix. Note pyrite coating and dolomitization. Bottom right: SEM image of 3-D fracture surface LGW7. Note pyrite and gypsum precipitates.

4. Experimental Device and Method

Fracture flow and stiffness tests were performed at the Norwegian Geotechnical Institute (NGI). Details about the equipment and standard procedures for testing are given in Berre (2011). In the current test program, isotropic loading conditions were applied to all the specimens through oil pressure in the main pressure chamber and all plugs were tested in its natural, intact state without splitting the fracture open. The horizontal strain was measured by two sensors, each sensor consisting of a submersible linear variable differential transformer
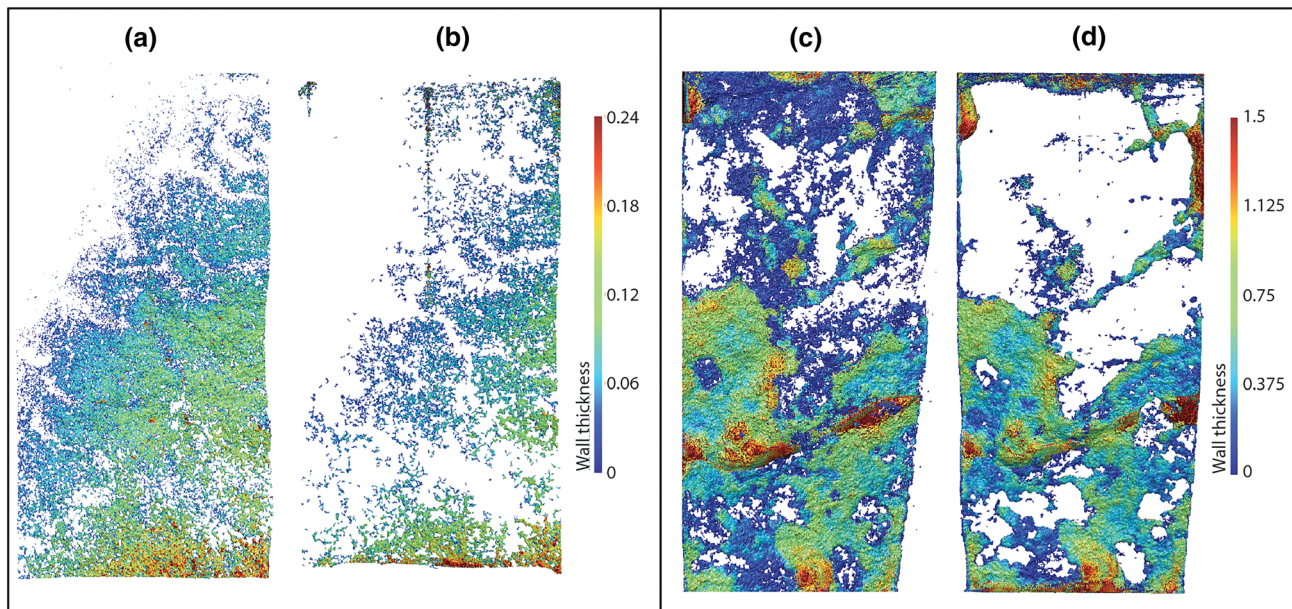

Figure 4. Surface plots of aperture (wall thickness) distribution in mm in samples before (pretest) and after the experiments (posttest) and no pressure confinement. The white spaces have thickness/aperture below CT scanner resolution (voxel resolution is 30 μm) and represent the contact area R_c. (a) LGW1 (pretest), (b) LGW1 (posttest), (c) LGW7 (pretest), and (d) LGW7 (posttest).

Table 2
Fracture Characteristics Derived From Pretest and Posttest CT Volume Reconstruction With No Pressure Confinement

Sample	Mean mech. aperture (mm)	Contact area, R_c (%)	Fracture surface roughness	Dense mineral ratio fracture/all sample (%)
LGW1-pre	0.10	36	Smooth	20
LGW1-post	0.09	59	Smooth	23
LGW7-pre	0.53	14	Rough	99
LGW7-post	0.44	44	Rough	98

(LVDT) fixed in a very light metal ring, which encloses the specimen. One horizontal strain sensor measured the change in diameter at the lower third point of the specimen height, and the other measured the change in diameter at the upper third point. The two diameters were oriented orthogonal to each other, and the sensors were placed such that the sensor Rad4 was measuring across the fracture, whereas the sensor Rad5 was measuring along the fracture for the two fractured samples LGW1 and LGW7 (Figure 5). Sensor placement is similar for the intact samples tested, LGW2 and LGW8. The internal local measurement of vertical strain was obtained by recording the change in distance between the two horizontal strain sensors using two vertical LVDT sensors. Volumetric strain was calculated from the deformation measurements.

4.1. Experimental Procedure

Experimental conditions are planned to reflect the shallow depth of samples (Table 1) by using 1 MPa initial effective confinement as the initial conditions, whereas the maximum effective loading of 9 MPa represents the stress range for overburden down to around 1,000 m. Initially, for each experiment (fractured and intact sample) a total confining pressure of 1 MPa was applied to the sample as part of the mounting procedure. The samples were then saturated with brine (35 g/L NaCl), amounting to similar concentrations as in situ brines (Kampman et al., 2013, 2014). Pore pressure and confining pressure were raised simultaneously to 10 and 11 MPa, respectively. After stabilization, samples were isotropically loaded under drained conditions, maintaining a backpressure of 10 MPa and increasing the confining pressure in steps (loading rate 0.3– 1.0 MPa/hr) up to 19 MPa. The samples were then unloaded in steps using the same loading rate, and for three of the four tests the load cycle was repeated to examine hysteresis effects. At every load step, after allowing some time for dissipation of potential excess pore pressure from the loading, the flow properties of the sample were measured using the constant head method. An appropriate pore pressure gradient was established across the specimen and steady-state flow measured using brine. For the permeable fractures, gradients in the range 0.01– 0.5 MPa were used, whereas gradients of 0.5–4.0 MPa were needed for intact samples. All gradients are applied adjusting both inlet and outlet pressure and maintaining a constant confining pressure at center of sample. After flow measurement, loading to the next step was commenced directly. The confining stress path for the various samples and cycles is shown in Figure 6. The total duration of each test varied from 20 to 80 days, depending on the time to achieve approximately steady-state conditions in the samples during flow measurements. After finishing the test and retrieving the specimen from the pressure vessel, the fractured specimens were gently pushed out of the membrane and moved to the X-ray CT scanner. The intact samples were immediately weighed and dried for determination of the porosity estimates (Table 1). The experiments focused on mechanical changes and no attempts were made to measure alteration of flow properties due to dissolution/precipitation or redox reactions during the test.
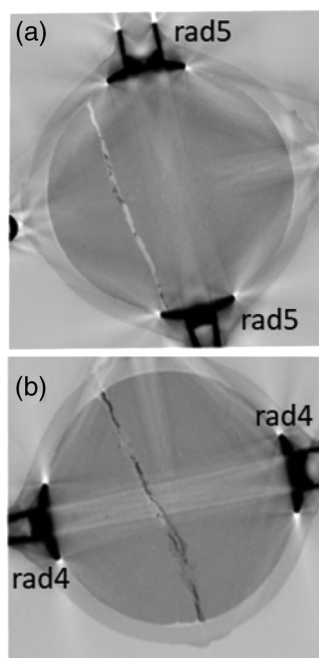
5. Experimental Results

5.1. Host Rock Bulk Properties

For both fractured samples, LGW1 and LGW7, two corresponding intact reference plugs, LGW2 and LGW8, were tested to establish the elastic
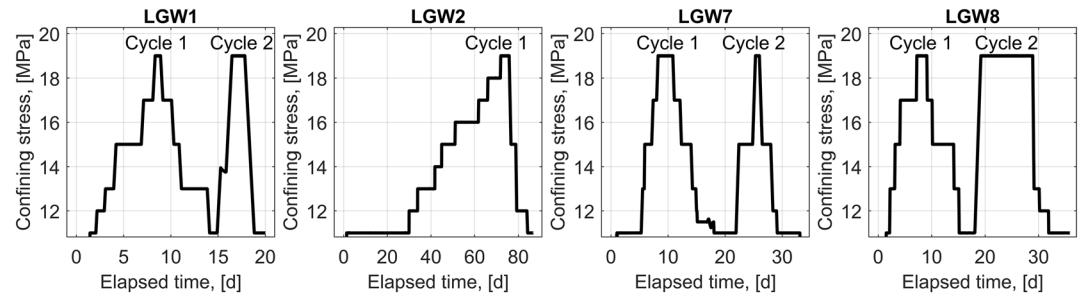

Figure 5. X-ray image of sample showing placement of the radial deformation sensors. Rad5 measures deformation along the fracture (a) and rad4 measures deformation across the fracture (b).

Figure 6. Total confining stress variation with time for the different tests. Backpressure was 10 MPa.

and flow properties of the host rock material as a reference. The isotropic loading cycles of the two intact samples showed comparable drained bulk modulus in the range of 1.5–3 GPa for the tested pressure range of 1–9 MPa effective stress (corresponding to a compressibility of 0.2–0.7 GPa^{-1}), whereas a slight difference in permeability is observed (Table 3). The measured intact drained bulk modulus is in the same order as the drained bulk modulus of 6.6 GPa reported for the Berea sandstone (Hart & Wang, 1995), a typical reference sandstone.

5.2. Fracture Stiffness

In order to derive the fracture stiffness, stress-dependent sample deformation during the first loading cycle was compared for the fractured and the intact sample couplets LGW1/LGW2 (Figure 7a) and LGW7/LGW8 (Figure 7b). Data from the two radial deformation sensors, Rad4 and Rad5, are plotted separately. For the intact samples, the two sensors show comparable deformation, whereas for the fractured samples LGW1 and LGW7, the deformation sensor parallel to fracture (Rad5) is close to or similar to the intact sample deformation. The sensor measuring across the fracture (Rad4) shows more deformation. Fracture deformation is defined by Bandis et al. (1983) as total measured deformation minus the intact deformation. Hence, the mechanical fracture deformation d_f or change in mechanical aperture Δb_M for the current samples can be defined as follows:

$$d_f = \Delta b_M = d_{Rad4} - d_{Rad5} \tag{6}$$

assuming that d_{Rad5} represents the intact rock deformation and d_{Rad4} can represent the combined fracture and intact deformation. The calculated fracture deformation d_f for the thin LGW1 fracture is less than the horizontal deformation measured on the corresponding host rock sample, LGW2 (Figure 7a), whereas for the wide fracture in LGW7 the calculated fracture deformation is larger than the horizontal deformation of the intact sample, LGW8 (Figure 7b). During loading Cycle 2, the fracture deformation for LGW 7 is below the deformation in the intact sample, similar to LGW1 (Figure 7c).

Due to loading pauses during the flow testing, the fracture deformation (Figure 7) is divided into loading intervals and fracture stiffness K_n (Equation 6) can be derived using three different calculation approaches (Figure 8a): (I) Continuous stiffness development using 0.2 MPa loading steps within the loading intervals. This approach gives a high-resolution stiffness development for each loading interval; however, the stiffness development is dominated by the stiffness reduction following the loading pause and only the final part of the curve shows the expected increase in stiffness with loading. (II) Average stiffness value calculated for each loading interval based on secant values for the deformation. This approach shows a stress-dependent linear increase in fracture stiffness with increasing effective stress. (III) Average stiffness value for each loading step based on secant values for deformation including the secondary creep in the sample. A linear increase in fracture stiffness is observed but with lower stiffness values than average for the loading interval.

Comparing the fracture stiffness K_n for the two samples LGW1 and LGW7 during first loading, unloading and second loading show the range of fracture stiffnesses that can be derived from the tests
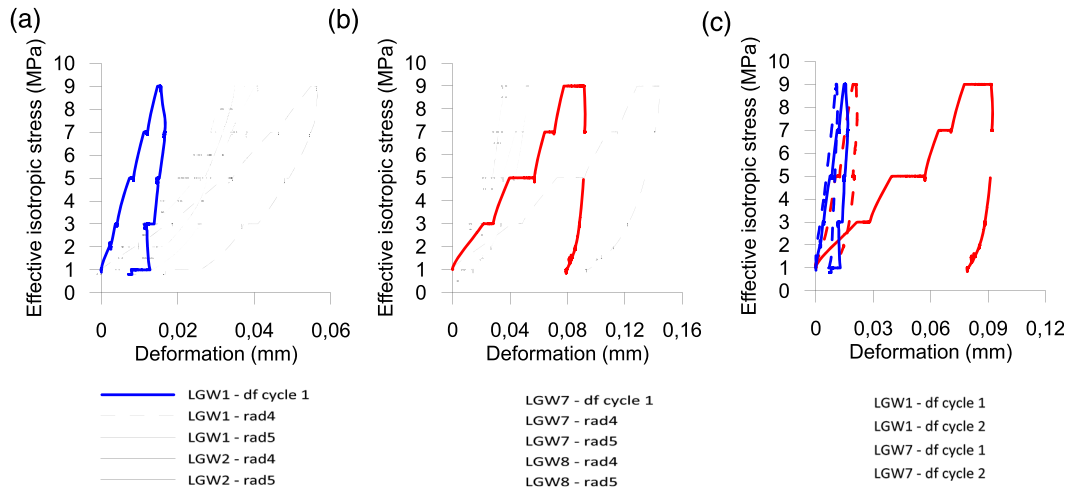
Table 3
Host Rock Bulk Modulus, Compressibility, and Flow Properties for the Effective Stress Conditions of 1–9 MPa Tested

Sample	Bulk modulus (GPa)	Compressibility (GPa^{-1})	Plug permeability (μD)
LGW2	1.5–3	0.3–0.7	0.03–0.09
LGW8	1.5–3	0.3–0.7	0.1–3.6

Note. The range in values reflects the stress dependency; bulk modulus increases with effective stress, and compressibility and permeability decrease with effective stress. Note that the bulk modulus and compressibility are reported for the loading phase only.

Figure 7. Fracture deformation d_f derived for first loading cycle for the red unbleached sandstone LGW1 and LGW2 (a) and for the bleached sandstone LGW7 and LGW8 (b). Comparison of fracture deformation for first and second loading (c).

(Figure 8b). The thin LGW1 fracture shows a higher stiffness than the wider LGW7 fracture both during first loading and reloading, whereas the unloading stiffness is higher for LGW7 fracture at early unloading steps but becomes lower than for LGW1 at low effective stresses. The calculated stiffness values for both LGW1 (400–800 MPa/mm) and LGW7 (100–300 MPa/mm) are in the same range as the normal fracture stiffness of 100–760 MPa/mm reported for sandstone by Chen et al. (2017).

5.3. Flow Measurements

During pauses in loading, steady-state volumetric flow rates using brine were measured for all four samples quantifying the fluid transport resulting from a constant pressure difference between the top and bottom of the samples. Stress-dependent flow properties, where flow decreases with increasing stress and increases with decreasing stress, are most prominent for the pale-colored samples (LGW7 and LGW8) during load Cycle 1, whereas for load Cycle 2 the stress dependency is much smaller (Figure 9a). The measured flow properties show good correlation with volumetric strains (Figure 9b). Exception from the general stress dependency observed is the abrupt decrease in flow during loading from 7 to 9 MPa effective stress in sample LGW1. This abrupt decrease is unrelated to deformation in the sample but might be explained as a fracture
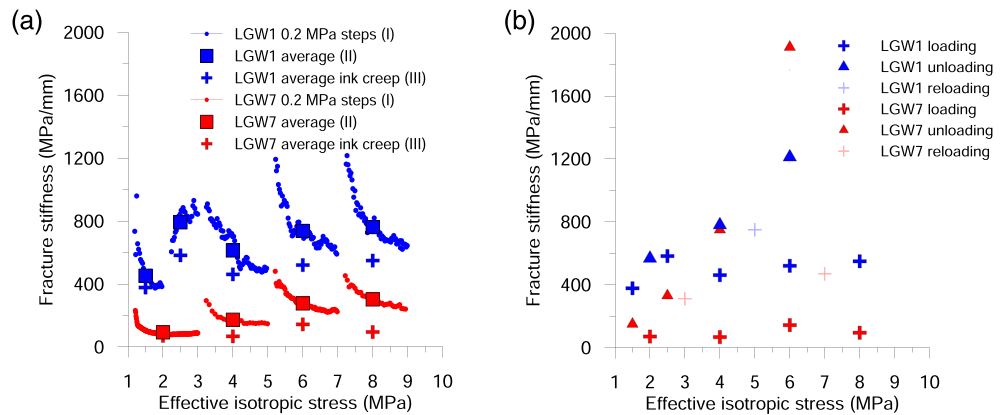

Figure 8. (a) Fracture stiffness as a function of effective isotropic stress condition calculated using three different approaches, (I) 0.2 MPa pressure steps, (II) average for loading interval, and (III) average including creep deformation. (b) Fracture stiffness including creep deformation for loading, unloading, and reloading. Lines are added to guide the trends.
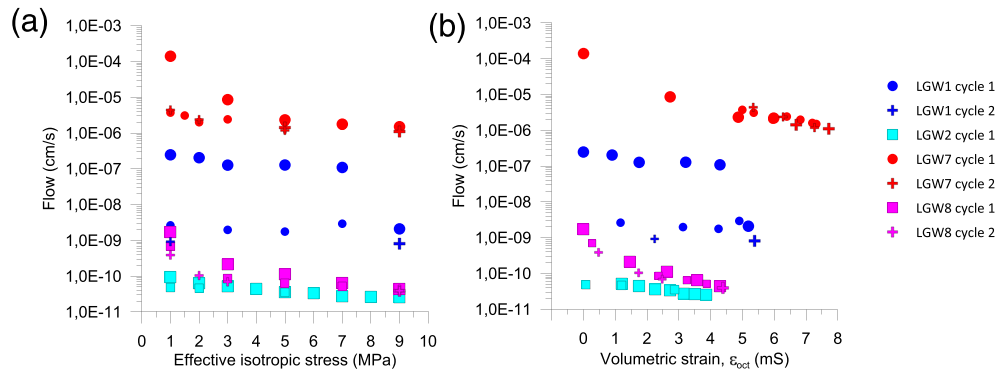
Figure 9. Comparing flow measurements for the two fractures plugs (LGW1 and LGW7) with the two intact plugs (LGW2 and LGW8). (a) Measured flow velocity as a function of effective stress and (b) flow as function of volumetric strain. Larger symbols are for the loading phase and smaller symbols are for the unloading phase.

closure, possibly from mating of the fracture surfaces or by particle clogging of the limited aperture near the top of the sample (Figures 9a and 9b).

The effective sample permeability k for intact and fractured samples is calculated from the volumetric flow rate measured in the tests using Darcy's law with effective flow area equal the cross-sectional area of the sample. Ratio of effective fractured plug permeability to intact plug permeability is in the order of $>10^3$ (Figure 10a), and it is therefore a good approximation to assume that measured flow rate, Q, in the fractured cores (LGW1 and LGW7) is mainly through the fracture. Based on this assumption, the hydraulic aperture b_H can be calculated using Equation 2 and the cross-sectional area approximated as $A = b_H w$, where w (m) is the width of the fracture set as the sample's diameter. The hydraulic aperture shows higher stress dependency for the LGW7 fracture compared to LGW1 (Figure 10b). Calculated hydraulic aperture ranges from 4 to 0.5 μm for LGW1 and LGW32 to 6 μm for LGW7 (Table 4), significantly lower than the mechanical aperture estimated from CT images in Table 2.

The temporal pressure, flow, and deformation profiles from the permeability tests show local stress distributions within each sample. An overview of applied pressure gradients is given in Figure 11a showing increasing pressure gradient with increasing confining stress. Intact samples display the steepest gradients. Volumetric flow development and radial deformation are included for the permeability test in the fractured LGW1 sample at an effective confinement of 3 MPa (Figure 11b) and 9 MPa (Figure 11c). Pore pressure is increased at the inlet, reduced at the outlet, and kept constant through the center of the plug. Corresponding changes in effective pressure conditions stress change are limited compared to pressure step between tests care that has been taken to allow for the new pore pressure to equalize before permeability is calculated from the steady-state phase. Both tests show a transient phase before steady-state flow conditions
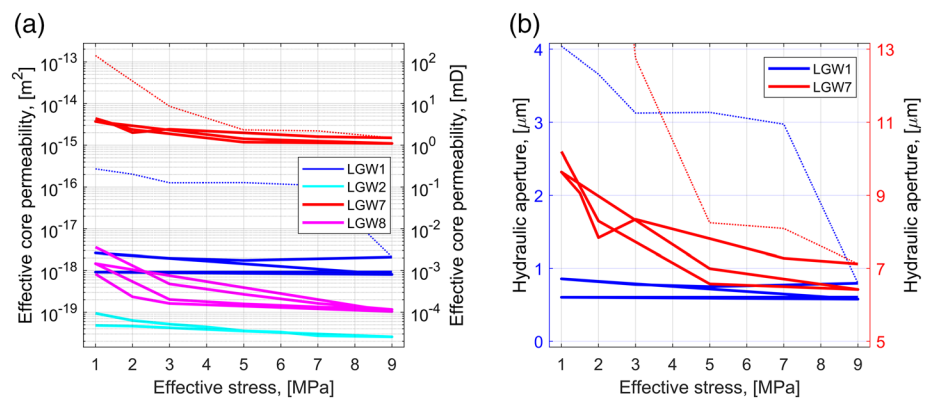

Figure 10. (a) Effective plug permeability. (b) Hydraulic aperture calculated from Equation 2 assuming zero contact ratio ($R_c = 0$). Maximum value for LGW1 in the first loading cycle (outside graph) is 32.3 μm. Dotted thin lines in both plots are from the first loading cycle.

Table 4
Core Permeability Variations Identified by Comparing Fractured Plugs With Host Rock Plugs

Sample	Initial plug permeability	Plug permeability at maximum loading, cycle 1	Plug permeability range, cycle 2	Hydraulic aperture range, cycle 1	Hydraulic aperture range, cycle 2
LGW1 (fractured)	0.27 mD	2 μD	0.8–0.9 μD	4–0.9 μm	0.9–0.6 μm
LGW2 (intact)	0.09 μD	0.03 μD	0.03–0.05 μD	—	—
LGW7 (fractured)	140 mD	1.5 mD	1.1–4.4 mD	32–7 μm	10–6 μm
LGW8 (intact)	3.6 μD	0.11 μD	0.1–1.5 μD	—	—

Note. Calculated hydraulic aperture uses the parallel plate model and assuming all flow in the fracture.

are reached. The first transient phase starts immediately after the gradient is imposed, and it is recognized by unstable flux in and out of the sample as well as onset of radial compression for the 9 MPa confinement test. A second, transient phase is identified based on sample deformation. Compression of the sample is observed for the 9 MPa confinement test, whereas at 3 MPa confinement, a very small dilation is observed. There is no observed effect of the deformation on the volumetric flow in this second transient phase. Steady-state flow conditions for the sample are achieved after 35 min for the test at 3 MPa and after 800 min for the 9 MPa test.

6. Discussion

The experimental program was designed to measure the stress-dependent flow properties for two natural occurring fractures characterized by their differences in natural fracture surface alteration from reactive paleo-flow within the LGW fault. A major concern for the experiments has been the long-term (weeks to months) exposure to brine during flow testing and the potential for fluid-rock interaction during the experiments influencing the measured flow and stiffness properties. Chemical monitoring of outlet fluid in the experiments has not been included, and potential mineral dissolution cannot be addressed directly. The measured fracture closure (Figures 7 and 8) and stress-dependent flow (Figure 9) are in line with fundament understanding of
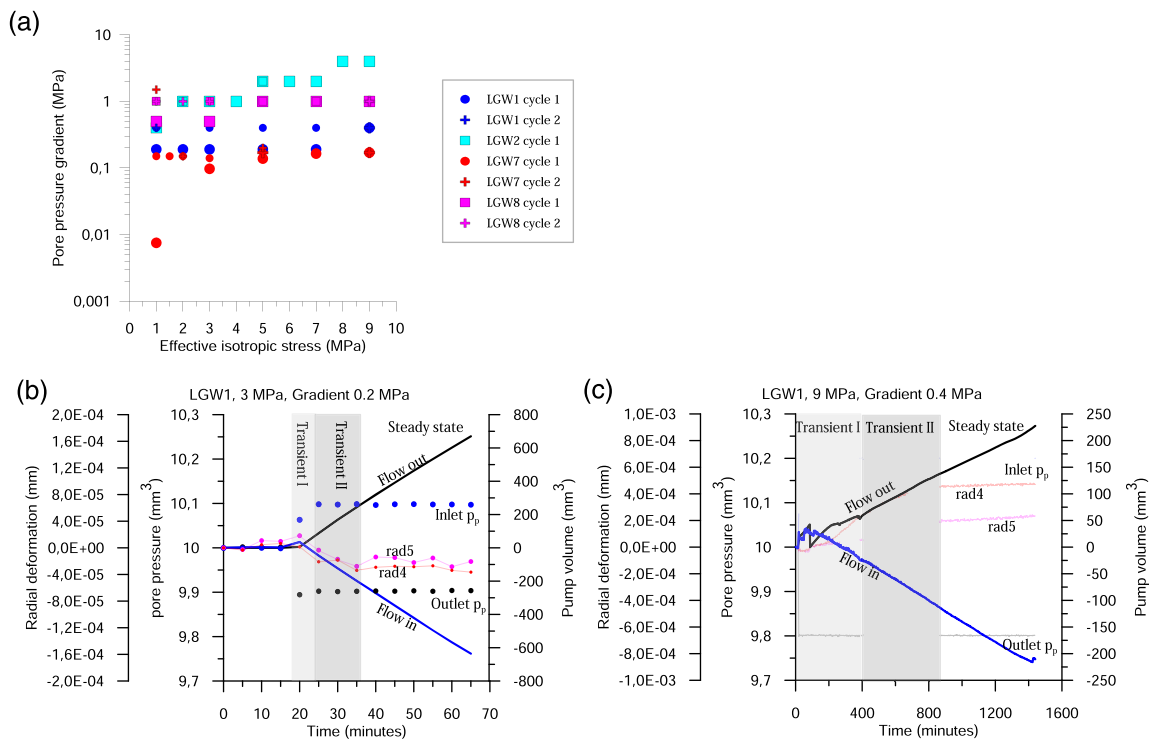

Figure 11. (a) Pore pressure gradient used during permeability measurements. Temporal development in pressure, flow, and radial deformation for permeability test on LGW1 fracture at 3 MPa confinement with 0.2 MPa pressure gradient (b) and LGW1 fracture at 9 MPa confinement with 0.4 MPa pressure gradient (c). Blue curves are pore pressure and pump volume at sample inlet, whereas black curves are for the outlet at the top. The red and magenta curves are the radial deformation sensors, rad4 and rad5, where positive values are compression and negative dilation.

stress-dependent elastic and permanent deformation on joints (Bandis et al., 1983). Compaction and mechanical closure of fracture aperture is the dominating mechanism in the shallow crust as reviewed by Jiang et al. (2010) and likely dominating this experimental work where stress conditions are representative for upper 1 km of the crust. Potential dissolution of asperities might contribute to the permanent mechanical fracture closure (Detwiler, 2008). In our experiment, carbonates and gypsum have the potential for dissolution during exposure to an undersaturated brine (Palandri & Kharaka, 2004); however, gypsum is only sporadically observed on the fracture surface and carbonate is found as cement within the low permeable matrix. The asperities are mainly pyrite and grain skeleton quartz with limited solubility under prevailing conditions. Hence, the effects of experimental related reactions are considered minor compared to the stress-related mechanical closure and we believe that it is relevant to relate the measured difference in fracture stiffness and flow for the tested samples to different natural in situ alteration within the fault zone.

Geochemical characterization of the samples and fracture surfaces is performed on samples not used in the experimental work providing details on in situ, paleo fluid-rock alteration effects form the LGW fault. The very prominent color difference between the two sample couplets tested (Figure 1) can be explained by minor differences in content and distributions of Fe oxides/hydroxides (Figure 2), as only a fraction of a percent of iron oxide is required to stain a sandstone red (Beitler et al., 2005). Different facies in the host rock may display various amounts of initial grain coating and/or pore-filling Fe oxides. However, the tested samples are form the same facies (Figure 1), and the pale samples LGW7 and LGW8 are considered to have been bleached due to previous fluid-rock interaction within the LGW fault. The inherent, red Fe staining in the host rock in samples LGW1 and LGW2 and the lack of precipitates on the fracture surface suggest limited or no reactive fluid circulation within this part of the LGW fault. In contrast, the bleached LGW7 sample has extensive pyrite precipitation on the fracture surface (Figure 3) as well as within the near-fracture matrix. Association with Ti-oxide (rutile/anatase) supports pyrite precipitation as an effect of reduction (i.e., bleaching), driving alterations with sulfur sourced from gypsum and/or formation water (Wigley et al., 2012). Further, the carbonate content in LGW7 is lower than in LGW1 and LGW8 (Figure 2), indicating paleofluid alteration processes including dissolution of carbonate (Aman et al., 2018). Relative solubility of carbonates depends on the fluid composition, as well as pressure and temperature conditions, but may be significant even on relatively short timescales in CO_2-rich fluid systems (Weibel et al., 2014) such as observed in the Green River area of Utah (e.g., Wigley et al., 2012). The observed fluid-rock alteration effects indicate that the LGW7 fracture has provided an important flow path within the LGW fault damage zone, and the measured geomechanical properties are representative of a fracture exposure to reactive, CO_2-charged brines within a fault in the overburden of a natural CO_2 reservoir (Kampman et al., 2014).

An important observation from this study is that the geochemical alterations which caused bleaching in the past have nondetectable effects on the measured current (resulting) host rock stiffness, presented as bulk modulus and compressibility in Table 3. However, the two fractures through bleached and unbleached fine-grained sandstones show very different stiffness properties that can be linked to paleofluid exposure and past geochemical alterations in fractures within the fault (Figure 3). The wide and rough LGW7 fracture shows a low fracture stiffness and a low contact ratio that may be linked to the large aperture controlled by mineral precipitates keeping the fracture open and preventing good mating of the fracture surfaces during closure. The unaltered, smoother LGW1 fracture shows a high fracture stiffness and high contact ratio likely related to several host rock bridges and good mating of the unaltered fracture surfaces. Relating the measured fracture stiffness to the contact area is in line with findings discussed in literature where fracture-specific stiffness depends critically on the extent of contact area (e.g., Brown & Scholz, 1985; Pyrak-Nolte & Morris, 2000), although the spatial distribution of contact points may also be of importance.

A flow-stiffness relationship is plotted based on the flow directly measured in the laboratory at the end of a loading interval covering the measured range of stiffness form 100–800 MPa/mm (Figure 12). Two main trends can be observed in the current data set: (I) a fast decay in flow with stiffness for the first loading of the LGW7 sample, whereas (II) for the LGW7 second loading and for LGW1, flow is less dependent on stiffness. The observed trends correspond well with the two main trends identified by Pyrak-Nolte and Morris (2000): a rapid decrease in flow for increasing fracture stiffness and a slow decrease of flow with increasing stiffness. Pyrak-Nolte and Morris (2000) show how the two trends are related to the spatial correlation of the aperture distribution and suggest that fractures with uniformly distributed contact areas show a
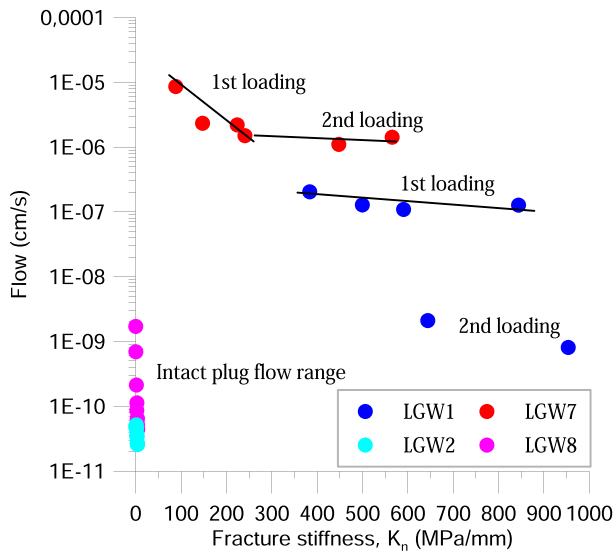
Figure 12. Fracture flow at end of loading interval as a function of fracture stiffness (calculated using Method I) and intact plug flow measurements included for comparison. Black lines are inserted to guide the trends.

slow decrease in flow with increasing stiffness due to multiple flow paths, whereas a more irregular contact surface distribution provides fractures with few dominant flow paths, which are more sensitive to stress changes. We find it interesting to observe that natural fracture surface alteration related to CO_2-saturated flow conditions in a fault may provide such a marked impact on the stiffness-flow relationship, although more work and detailed investigations are needed to further discuss this effect.

Unique for these fracture flow and stiffness experiments are that the naturally fractured samples were not separated for fracture surface characterization before testing. Both samples were kept together as they were in situ during drilling and sample preparation, held in place by minor rock bridges, and/or precipitates within the fracture. Thus, the natural fit between the two fracture surfaces has been kept in place throughout the test, suggesting that actual fracture apertures representative for natural, in situ conditions are tested. The measured permeability decay with increasing normal load shows a high stress dependency for the large aperture in the altered LGW7 facture and less stress dependency for the un-altered LGW1 fracture (Figure 9). Interestingly, the altered LGW7 fracture maintains a high flow rate compared to the host rock during loading, whereas flow within the unaltered LGW1 fracture approaches the host rock permeability range during similar loading. Our interpretation is that unaltered fracture surfaces like LGW1 are smoother and better mated with a potential to fully close and reseal, whereas the fractures that have been altered by CO_2-charged brines within the LGW fault display a rougher surface and cannot be mechanically closed with the same loading. This is an important observation with respect to calculate the total leakage potential through a prospective rock reservoir succession, as the type of mineral precipitates, grain dissolution, grain shapes, and distribution may influence the fracture closure and flow.

7. Conclusion

The new experimentally defined stiffness and flow relationships presented in this study supplement the need for better understanding of natural fractures within siliciclastic rocks and quantification of inherent effects of natural fluid-rock alterations. Combining experimental data and detailed geochemical characterization provides unique opportunities for interpretation and discussion of natural fracture stiffness and fluid flow properties in a fracture system within the damage zone of the LGW fault. Fracture stiffness and flow properties are measured and compared for a nonaltered, small aperture fracture (LGW1) and a strongly altered, wide aperture fracture (LGW7). Key observations are as follows:

1. High fracture stiffness of 400–800 MPa/mm and flow approaching the measured μD host rock permeability are observed for the small aperture fracture during loading, whereas low fracture stiffness of 100–300 MPa/mm and fracture permeability 4 orders of magnitude higher than the host rock are observed for the wide aperture fracture.
2. The measured difference in fracture stiffness and flow properties is attributed to in situ exposure and reaction to CO_2-saturated brines within the LGW fault causing bleaching, dissolution, and mineral precipitation.
3. The altered and wide fracture from the bleached core section shows carbonate dissolution and pyrite precipitates giving a low contact ratio and irregular aperture distribution with poor mating making the fracture difficult to close, and it maintains a considerable flow during loading.
4. The nonaltered small aperture fracture from the inherent red core section shows high contact ratio and several host rock bridges that easily mate, close, and approach host rock flow conditions during loading.

Appendix A: Sedimentary Facies

The sedimentary facies described for the Entrada Sandstone in well CO_2W55 is presented in Table A1 together with facies associations.

Table A1
Facies Description for Entrada Sandstone, Well CO₂W55

Facies	Description	Interpretation	Facies associations
A	Pale red to rusty-red, structureless sandy silt deposits. Bleached zonations along fractures occurring locally	Damp/wet, desert margin, loess and aeolian sandstone, structureless texture potentially linked to fluidization of the sediments	FA 1—Paralic coastal plain at the margin of a wet aeolian desert, on which superficial soil occasionally developed; recurrent (marine) flooding possible (see Zuchuat, Sleveland, et al., 2019)
B	Pale red to rusty-red, plane parallel-laminated silt to fine-grained sandstone. Bleached zonations along fractures occurring locally	Damp/wet, desert margin, loess and aeolian sandstone deposited quasi-planar adhesion in a wet/damp sand (Hunter, 1980). Undisturbed as opposed to Facies A	
C	Dark rusty-red, muddy, very fine to fine-grained, mottled, sandstone. Bleached halos associated with bioturbations can occur, as well with evaporite-rich patches	Immature, rhizolithic soil profiles. Bleached halos are linked to the circulation of organic acids through the tight mudstones along the rhizoliths (Blodgett, 1988). Evaporite precipitation occurred during dry periods	
D	Fine-grained sandstone with unidirectional, current ripples cross stratification	Translatent wind ripple migrating over a plane to near-plane surface (Kocurek, 1981)	Transition between FA 1 and FA 2
E	White, very fine to fine-grained sandstone with steep, tabular, 1–2 m thick tangential cross stratification. Sharp base, potentially erosive, fining upward trends scarcely observed	Migrating, sinous-creseted (3-D), isolated, coastal dune (Hunter, 1977; Zuchuat, Midtkandal, et al., 2019; Zuchuat, Sleveland, et al., 2019)	FA 2—coastal aeolian dunes at the margin a of wet aeolian desert, migrating on top of FA 1 (see Zuchuat, Sleveland, et al., 2019)
F	White, fine- to medium-grained sandstone, with low angle, undulating to plane parallel-stratification. Unidirectional current ripples scarcely observed	Toesets of migrating, sinous-creseted (3-D), isolated, coastal dunes (Hunter, 1977; Zuchuat, Midtkandal, et al., 2019; Zuchuat, Sleveland, et al., 2019)	

Appendix B: XRD Data

X-ray powder diffraction (XRD) data are measured on side material for sample LGW2, LGW7, and LGW8. The results are presented in Figure B1.
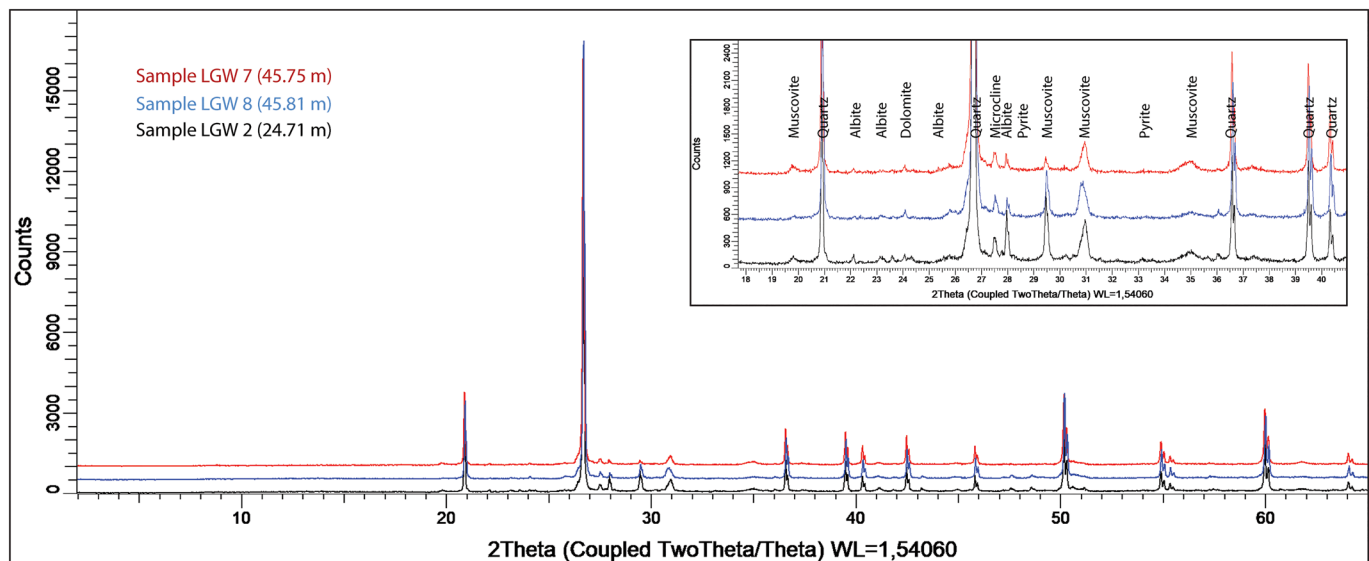

Figure B1. X-ray powder diffraction (XRD) data for sample LGW2, LGW7, and LGW8.

Data Availability Statement

The experimental data are published at DataverseNO. Skurtveit, Elin; Soldal, Magnus, 2020, "Replication Data for: Experimental investigation of natural fracture stiffness and flow properties in a faulted CO_2 bypass system (Utah, USA)", https://doi.org/10.18710/I6FB4N, DataverseNO, V1.

References

Aman, M., Espinoza, D. N., Ilgen, A. G., Major, J. R., Eichhubl, P., & Dewers, T. A. (2018). CO_2-induced chemo-mechanical alteration in reservoir rocks assessed via batch reaction experiments and scratch testing. *Greenhouse Gases: Science and Technology*, *8*(1), 133–149. https://doi.org/10.1002/ghg.1726

Bandis, S., Lumsden, A., & Barton, N. (1983). Fundamentals of rock joint deformation. *International Journal of Rock Mechanics and Mining Sciences & Geomechanics Abstracts*, *20*(6), 249–268.

Barton, N., & Choubey, V. (1977). The shear strength of rock joints in theory and practice. *Rock Mechanics*, *10*(1–2), 1–54. https://doi.org/10.1007/BF01261801

Beitler, B., Parry, W. T., & Chan, M. A. (2005). Fingerprints of fluid flow: Chemical diagenetic history of the Jurassic Navajo Sandstone, southern Utah, USA. *Journal of Sedimentary Research*, *75*(4), 547–561. https://doi.org/10.2110/jsr.2005.045

Berre, T. (2011). Triaxial testing of soft rocks. *Geotechnical Testing Journal*, *34*(1), 61–75.

Blodgett, R. H. (1988). Calcareous paleosols in the Triassic Dolores Formation. *Paleosols and weathering through time—principles and applications: Geological Society of America Special Papers*, *216*, 103–121. https://doi.org/10.1130/SPE216-p103

Bohloli, B., Ringrose, P., Grande, L., & Nazarian, B. (2017). Determination of the fracture pressure from CO_2 injection time-series datasets. *International Journal of Greenhouse Gas Control*, *61*, 85–93. https://doi.org/10.1016/j.ijggc.2017.03.025

Brown, S. R., & Scholz, C. H. (1985). Closure of random elastic surfaces in contact. *Journal of Geophysical Research*, *90*(B7), 5531–5545. https://doi.org/10.1029/JB090iB07p05531

Busch, A., Kampman, N., Hangx, S., Snippe, J., Bickle, M., Bertier, P., et al. (2014). The Green River natural analogue as a field laboratory to study the long-term fate of CO_2 in the subsurface. *Energy Procedia*, *63*, 2821–2830. https://doi.org/10.1016/j.egypro.2014.11.304

Campbell, A. J., & Baer, L. J. (1978). Little Grand Wash fault—Crystal Geyser area (CO_2 gas), T. 21-22 S., R. 15-17 E., grand and Emery counties, Utah. *Oil and Gas Fields of the Four Corners Area* (Vol. I–II).

Chan, M. A., Parry, W., & Bowman, J. (2000). Diagenetic hematite and manganese oxides and fault-related fluid flow in Jurassic sandstones, southeastern Utah. *AAPG Bulletin*, *84*(9), 1281–1310.

Chen, Y., Liang, W., Lian, H., Yang, J., & Nguyen, V. P. (2017). Experimental study on the effect of fracture geometric characteristics on the permeability in deformable rough-walled fractures. *International Journal of Rock Mechanics and Mining Sciences*, *98*, 121–140. https://doi.org/10.1016/j.ijrmms.2017.07.003

Detwiler, R. L. (2008). Experimental observations of deformation caused by mineral dissolution in variable-aperture fractures. *Journal of Geophysical Research*, *113*, B08202. https://doi.org/10.1029/2008JB005697

Dippenaar, M. A., & Van Rooy, J. L. (2016). On the cubic law and variably saturated flow through discrete open rough-walled discontinuities. *International Journal of Rock Mechanics and Mining Sciences*, *89*, 200–211. https://doi.org/10.1016/j.ijrmms.2016.09.011

Eichhubl, P., Davatz, N. C., & Becker, S. P. (2009). Structural and diagenetic control of fluid migration and cementation along the Moab fault, Utah. *AAPG Bulletin*, *93*(5), 653–681. https://doi.org/10.1306/02180908080

Espinoza, D. N., Jung, H., Major, J. R., Sun, Z., Ramos, M. J., Eichhubl, P., et al. (2018). CO_2 charged brines changed rock strength and stiffness at Crystal Geyser, Utah: Implications for leaking subsurface CO_2 storage reservoirs. *International Journal of Greenhouse Gas Control*, *73*, 16–28. https://doi.org/10.1016/j.ijggc.2018.03.017

Evans, J. P., Heath, J., Shipton, Z. K., Kolesar, P. T., Dockrill, B., Williams, A., et al. (2004). Natural leaking CO_2-charged systems as analogs for geologic sequestration sites. *Paper presented at Third Annual Conference on Carbon Capture and Sequestration, Alexandria, VA*.

Fossen, H., Schultz, R. A., Shipton, Z. K., & Mair, K. (2007). Deformation bands in sandstone: A review. *Journal of the Geological Society of London*, *164*, 755–769. https://doi.org/10.1144/0016-76492006-036

Frery, E., Gratier, J.-P., Ellouz-Zimmerman, N., Deschamps, P., Blamart, D., Hamelin, B., & Swennen, R. (2017). Geochemical transect through a travertine mount: A detailed record of CO_2-enriched fluid leakage from Late Pleistocene to present-day–Little Grand Wash fault (Utah, USA). *Quaternary International*, *437*, 98–106. https://doi.org/10.1016/j.quaint.2016.09.035

Frery, E., Gratier, J.-P., Ellouz-Zimmerman, N., Loiselet, C., Braun, J., Deschamps, P., et al. (2015). Evolution of fault permeability during episodic fluid circulation: Evidence for the effects of fluid-rock interactions from travertine studies (Utah–USA). *Tectonophysics*, *651*, 121–137.

Garden, I., Guscott, S., Burley, S., Foxford, K., Walsh, J., & Marshall, J. (2001). An exhumed palaeo-hydrocarbon migration fairway in a faulted carrier system, Entrada Sandstone of SE Utah, USA. *Geofluids*, *1*(3), 195–213. https://doi.org/10.1046/j.1468-8123.2001.00018.x

Gratier, J.-P., Frery, E., Deschamps, P., Røyne, A., Renard, F., Dysthe, D., et al. (2012). How travertine veins grow from top to bottom and lift the rocks above them: The effect of crystallization force. *Geology*, *40*(11), 1015–1018. https://doi.org/10.1130/G33286.1

Hart, D. J., & Wang, H. F. (1995). Laboratory measurements of a complete set of poroelastic moduli for Berea sandstone and Indiana limestone. *Journal of Geophysical Research*, *100*(B9), 17,741–17,751. https://doi.org/10.1029/95JB01242

Hunter, R. E. (1977). Basic types of stratification in small eolian dunes. *Sedimentology*, *24*(3), 361–387. https://doi.org/10.1111/j.1365-3091.1977.tb00128.x

Hunter, R. E. (1980). Quasi-planar adhesion stratification: An eolian structure formed in wet ssand. *Journal of Sedimentary Research*, *50*(1), 263–266.

Huo, D., & Benson, S. M. (2015). An experimental investigation of stress-dependent permeability and permeability hysteresis behavior in rock fractures. *Fluid Dynamics in Complex Fractured-Porous Systems*, *99-114*. https://doi.org/10.1002/9781118877517.ch7

Inui, M., Umezu, N., Wakasaki, K., & Sato, S. (2015). Thickness and clearance visualization based on distance field of 3D objects. *Journal of Computational Design and Engineering*, *2*(3), 183–194. https://doi.org/10.1016/j.jcde.2015.04.001

Jaeger, J. C., Cook, N. G., & Zimmerman, R. (2009). *Fundamentals of rock mechanics*. New York, NY: John Wiley & Sons.

Jiang, X.-W., Wang, X.-S., & Wan, L. (2010). Semi-empirical equations for the systematic decrease in permeability with depth in porous and fractured media. *Hydrogeology Journal*, *18*(4), 839–850. https://doi.org/10.1007/s10040-010-0575-3

Jung, N.-H., Han, W. S., Watson, Z., Graham, J. P., & Kim, K.-Y. (2014). Fault-controlled CO_2 leakage from natural reservoirs in the Colorado Plateau, East-Central Utah. *Earth and Planetary Science Letters*, *403*, 358–367. https://doi.org/10.1016/j.epsl.2014.07.012

Kampman, N., Bickle, M., Maskell, A., Chapman, H., Evans, J., Purser, G., et al. (2014). Drilling and sampling a natural CO_2 reservoir: Implications for fluid flow and CO_2-fluid-rock reactions during CO_2 migration through the overburden. *Chemical Geology*, *369*, 51–82. https://doi.org/10.1016/j.chemgeo.2013.11.015

Kampman, N., Maskell, A., Bickle, M., Evans, J., Schaller, M., Purser, G., et al. (2013). Scientific drilling and downhole fluid sampling of a natural CO_2 reservoir, Green River, Utah. *Scientific Drilling*, *16*, 33–43. https://doi.org/10.5194/sd-16-33-2013

Kocurek, G. (1981). Significance of interdune deposits and bounding surfaces in aeolian dune sands. *Sedimentology*, *28*(6), 753–780. https://doi.org/10.1111/j.1365-3091.1981.tb01941.x

Lang, P. S., Paluszny, A., & Zimmerman, R. W. (2016). Evolution of fracture normal stiffness due to pressure dissolution and precipitation. *International Journal of Rock Mechanics and Mining Sciences*, *88*, 12–22. https://doi.org/10.1016/j.ijrmms.2016.06.004

Major, J. R., Eichhubl, P., Dewers, T. A., & Olson, J. E. (2018). Effect of CO_2–brine-rock interaction on fracture mechanical properties of CO_2 reservoirs and seals. *Earth and Planetary Science Letters*, *499*, 37–47. https://doi.org/10.1016/j.epsl.2018.07.013

Midtkandal, I., Sundal, A., Braathen, A., Petrie, E., Zuchuat, V., Skurtveit, E., et al. (2018). CO_2 seal bypass—A multidisciplinary approach to CO_2 migration and storage. *Paper presented at 14th Greenhouse Gas Control Technologies Conference, Melbourne, 21–26 October 2018 (GHGT-14)*. Available at SSRN: https://ssrn.com/abstract=3365552.

Naruk, S., Solum, J., Brandenburg, J., Origo, P., & Wolf, D. (2019). Effective stress constraints on vertical flow in fault zones: Learnings from natural CO_2 reservoirs. *AAPG Bulletin*, *103*(8), 1979–2008. https://doi.org/10.1306/12181817393

Ogata, K., Senger, K., Braathen, A., & Tveranger, J. (2014). Fracture corridors as seal-bypass systems in siliciclastic reservoir-cap rock successions: Field-based insights from the Jurassic Entrada Formation (SE Utah, USA). *Journal of Structural Geology*, *66*, 162–187. https://doi.org/10.1016/j.jsg.2014.05.005

Palandri, J. L., & Kharaka, Y. K. (2004). A compilation of rate parameters of water-mineral interaction kinetics for application to geochemical modeling (Open File Report 2004-1068). Menlo Park CA: U.S. Geological Survey.

Peterson, F. (1988). Pennsylvanian to Jurassic eolian transportation systems in the western United States. *Sedimentary Geology*, *56*(1–4), 207–260. https://doi.org/10.1016/0037-0738(88)90055-3

Pyrak-Nolte, L., & Morris, J. (2000). Single fractures under normal stress: The relation between fracture specific stiffness and fluid flow. *International Journal of Rock Mechanics and Mining Sciences*, *37*(1-2), 245–262. https://doi.org/10.1016/S1365-1609(99)00104-5

Pyrak-Nolte, L., & Nolte, D. (2016). Approaching a universal scaling relationship between fracture stiffness and fluid flow. *Nature Communications*, *7*(1), 10,663. https://doi.org/10.1038/ncomms10663

Rutqvist, J., & Stephansson, O. (2003). The role of hydromechanical coupling in fractured rock engineering. *Hydrogeology Journal*, *11*(1), 7–40. https://doi.org/10.1007/s10040-002-0241-5

Shipton, Z. K., Evans, J. P., Kirschner, D., Kolesar, P. T., Williams, A. P., & Heath, J. (2004). Analysis of CO_2 leakage through 'low-permeability' faults from natural reservoirs in the Colorado Plateau, east-central Utah. *Geological Society, London, Special Publications*, *233*(1), 43–58. https://doi.org/10.1144/GSL.SP.2004.233.01.05

Simpleware™ScanIP (2018), Version O-2018-SP2L: Synopsys, Inc., Mountain View, USA, edited.

Skurtveit, E., Braathen, A., Larsen, E. B., Sauvin, G., Sundal, A., & Zuchuat, V. (2017). Pressure induced deformation and flow using CO_2 field analogues, Utah. *Energy Procedia*, *114*, 3257–3266. https://doi.org/10.1016/j.egypro.2017.03.1457

Skurtveit, E., Choi, J. C., Mulrooney, M., Osmond, J. L., & Braathen, A. (2018). 3D fault integrity screening for Smeaheia CO_2 injection site. *Paper presented at 14th Greenhouse Gas Control Technologies Conference Melbourne 21–26 October 2018 (GHGT-14)*. Available at SSRN: https://ssrn.com/abstract=3366335 edited.

Sundal, A., Miri, R., Hellevang, H., Tveranger, J., Midtkandal, I., Zuchuat, V., et al. (2017). Movement of CO_2 charged fluids in low permeability rocks during deformation: Migration patterns in the Carmel Formation, Utah. *Energy Procedia*, *114*, 4537–4544. https://doi.org/10.1016/j.egypro.2017.03.1570

Vrolijk, P. J., Urai, J. L., & Kettermann, M. (2016). Clay smear: Review of mechanisms and applications. *Journal of Structural Geology*, *86*, 95–152. https://doi.org/10.1016/j.jsg.2015.09.006

Walsh, J. (1981). Effect of pore pressure and confining pressure on fracture permeability. *Paper presented at International Journal of Rock Mechanics and Mining Sciences & Geomechanics Abstracts, Elsevier*. https://doi.org/10.1016/0148-9062(81)90006-1

Weibel, R., Kjøller, C., Bateman, K., Laier, T., Nielsen, L., & Purser, G. (2014). Carbonate dissolution in Mesozoic sand-and claystones as a response to CO_2 exposure at 70°C and 20 MPa. *Applied Geochemistry*, *42*, 1–15. https://doi.org/10.1016/j.apgeochem.2013.12.006

Wigley, M., Kampman, N., Dubacq, B., & Bickle, M. (2012). Fluid-mineral reactions and trace metal mobilization in an exhumed natural CO_2 reservoir, Green River, Utah. *Geology*, *40*(6), 555–558. https://doi.org/10.1130/G32946.1

Witherspoon, P. A., Wang, J. S., Iwai, K., & Gale, J. E. (1980). Validity of cubic law for fluid flow in a deformable rock fracture. *Water Resources Research*, *16*(6), 1016–1024. https://doi.org/10.1029/WR016i006p01016

Zuchuat, V., Midtkandal, I., Poyatos-Moré, M., Da Costa, S., Brooks, H. L., Halvorsen, K., et al. (2019). Composite and diachronous stratigraphic surfaces in low-gradient, transitional settings: The J-3 "unconformity" and the Curtis Formation, east-central Utah, USA. *Journal of Sedimentary Research*, *89*(11), 1075–1095. https://doi.org/10.2110/jsr.2019.56

Zuchuat, V., Sleveland, A. R., Pettigrew, R. P., Dodd, T. J., Clarke, S. M., Rabbel, O., et al. (2019). Overprinted allocyclic processes by tidal resonance in an epicontinental basin: The Upper Jurassic Curtis Formation, east-central Utah, USA. The Depositional Record. https://doi.org/10.1002/dep2.69